J. Fluid Mech. (2003), *vol.* 479, *pp.* 259–286.
DOI: 10.1017/S0022112002003518 Printed in the United Kingdom

The wall-jetting effect in Mach reflection: theoretical consideration and numerical investigation

By L. F. HENDERSON[1], E. I. VASILEV[2], G. BEN-DOR[1] AND T. ELPERIN[1]

[1]Pearlstone Center for Aeronautical Engineering Studies, Department of Mechanical Engineering, Ben-Gurion University of the Negev, Beer Sheva, Israel

[2]Department of Computational Mechanics, Volgograd State University, Volgograd, Russia

(Received 6 November 2001 and in revised form 1 October 2002)

The jetting effect often appears in the Mach reflection of a shock and in more complicated irregular shock reflections. It also occurs in some natural phenomena, and industrially important processes. It is studied numerically using a W-modification of the second-order Godunov scheme, to integrate the system of Euler equations. It is shown that there is no correspondence between the shock reflection patterns and the occurrence of jetting. Furthermore, there are two kinds of jetting: strong which occurs when there is a branch point on the ramp surface where the streamlines divide into an upstream moving jet and a downstream moving slug; and weak which has no branch point and may occur at small and large values of the ramp angle θ_w. The width of the jet for Mach and other reflections is determined by the angle of the Mach stem at the triple point (also called the Mach node or three-shock node). Strong jetting is unstable and the primary instability is in the jet itself. The contact discontinuity is also unstable, but its instability is secondary with respect to the jet instability. Two types of irregular reflection are identified in the dual-solution-domain. They are a two-node system comprising a Mach node followed by a four-shock (overtake) node; and another which seems to be intermediate between the previous system and a three-node reflection, which was first hypothesized by Ben-Dor & Glass (1979). An approximate criterion for the jetting $\leftrightarrow$ no-jetting transition is presented. It is derived by an analysis of the system of Euler equations for a self-similar flow, and has a simple geometrical interpretation.

1. Introduction

The jetting effect is present in numerous phenomena of scientific and industrial interest. Jets are formed by the explosion of a shaped charge lined by metal (Birkoff *et al.* 1948; Meyers 1994); applications are to armour penetration and cutting of large-diameter pipes by line charges. Jetting often occurs on the impact of solids, such as the shallow-angle collision of two explosively driven flat plates (Walsh, Shreffler & Willing 1953; Rinehart & Pearson 1963), impact of meteorites on the moon, or the collision of asteroids in space where cooling jets produce glassy minerals, bronzite, dunite and quartz (Kieffer 1977), or the impact of liquid drops on hard surfaces (Springer 1976; Dear & Field 1986). The effect has been observed during the diffraction of shock waves over ramps in gases (Ben-Dor 1978; Glaz *et al.* 1985, 1986; Li & Ben-Dor 1999); during the refraction of shocks through gaseous interfaces

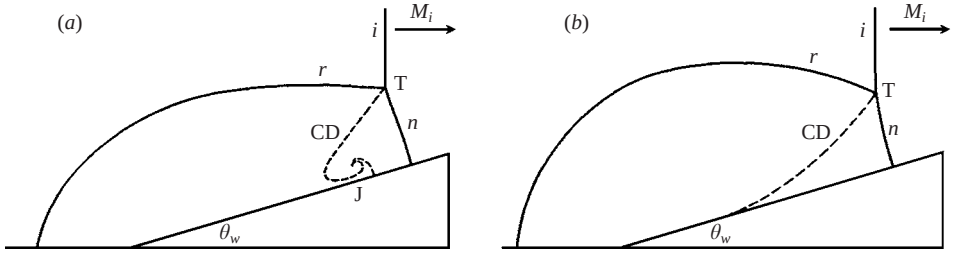

FIGURE 1. (*a*) The jetting and (*b*) no-jetting effects in SMR. *i*, incident shock wave; *r*, reflected shock wave; *n*, Mach shock (here called the *n*-shock); CD, contact discontinuity; T, triple point (Mach node); J, jet.

(Jahn 1956; Abdel-Fattah, Henderson & Lozzi 1976; Abdel-Fattah & Henderson 1978; Henderson, Colella & Puckett 1991); and in the collapse of bubbles during cavitation (Hammit 1980).

In this study, we present the results of a numerical and theoretical study of the effect as it appears in the diffraction of a shock over a ramp in a perfect gas. The governing parameters of the system are: γ, the ratio of specific heats, M_i, the Mach number of the incident (diffracting) shock wave, and θ_w, the ramp angle. It is well known that a single-Mach reflection (SMR) (figure 1) can occur when a shock diffracts over a ramp with a sufficiently small angle. The SMR system contains three shocks meeting at a point, called the triple-point or Mach node T (Glimm *et al.* 1985). Unless otherwise stated, this point will be simply called the node. Part of the fluid passes sequentially through the incident (*i*-shock) and the reflected (*r*-shock) waves (the *i*–*r* sequence), while the remainder passes only through the Mach stem (*n*-shock). Since by the triple-shock-entropy theorem (TSE) of Henderson & Menikoff (1998) the entropy in the fluid behind the *i*–*r* sequence is smaller than behind the *n*-shock, a contact discontinuity (CD) emanates from the node. By corollary 4 of the TSE-theorem and Bernoulli's theorem, the kinetic energy in a frame of reference attached to the triple point is greater for the *i*–*r* sequence. If M_i is sufficiently large, the part of the flow that passes through the *i*–*r* sequence and is bounded by the CD will turn upstream as it approaches the ramp surface and drive towards the *n*-shock, causing the jetting effect (figure 1*a*). The CD-boundary of the jet is displaced from the surface. If, however, M_i is sufficiently small, all the flow through the *i*–*r* sequence passes downstream and its CD-boundary becomes tangent to the ramp surface; this is referred to as the no-jetting effect (figure 1*b*).

2. Coordinates and notation

2.1. *Rest frame*

Consider an (x,y)- coordinate system attached to the ramp with origin O at the apex; the axis x coincides with the surface and y is perpendicular to it (figure 2). Let $\boldsymbol{D}_i$, $\boldsymbol{D}_r$ and $\boldsymbol{D}_n$ be the velocities of the *i*-, *r*- and *n*-shocks, respectively, and $\boldsymbol{U}_i$, $\boldsymbol{U}_r$ and $\boldsymbol{U}_n$ be the corresponding particle velocities. All the vectors refer to conditions at the Mach node, T. The vector magnitudes are denoted by normal (non-bold) founts, e.g. D_i, D_r and D_n. The *i*- and *n*-shocks travel distances D_i and D_n in a unit time as the node moves from O to T. Similarly, the particles travel the distances U_i or U_n in the same time. The $\boldsymbol{D}_r$ and $\boldsymbol{U}_r$ vectors move with the tip of $\boldsymbol{U}_i$. The tips of the $\boldsymbol{U}_i$ and $\boldsymbol{U}_n$ vectors touch the extended tangent to the contact discontinuity at T. Along the

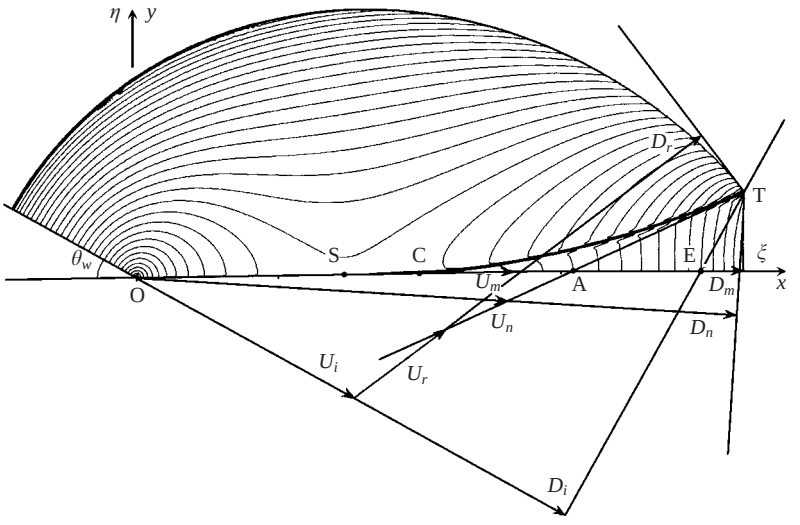

FIGURE 2. Definition of the velocities in an SMR wave configuration and isopycnics for $\gamma = 1.4$, $\theta_w = 30°$ and $M_i = 1.6$. A, intersection of the tangent to the contact discontinuity at the node with the ramp surface; C, the point where the contact discontinuity merges into the ramp surface; S, a stagnation point.

ramp surface, the n-shock velocity vector and the particle velocity vector behind it are denoted by $\boldsymbol{D}_m$ and $\boldsymbol{U}_m$.

The tangent to the contact discontinuity at T intersects the ramp surface at A; C is the point where the contact discontinuity merges into the ramp surface, and S is a stagnation point. Formally, we define the slug length to be the distance in unit time between the points S and C.

The mass, x-momentum, y-momentum and entropy conservation equations for an unsteady compressible flow of a perfect gas in (x,y)-coordinates, are, respectively,

$$\rho_t + (\rho u)_x + (\rho v)_y = 0, \tag{2.1a}$$

$$u_t + uu_x + vu_y + \rho^{-1} p_x = 0, \tag{2.1b}$$

$$v_t + uv_x + vv_y + \rho^{-1} p_y = 0, \tag{2.1c}$$

$$(p\rho^{-\gamma})_t + u(p\rho^{-\gamma})_x + v(p\rho^{-\gamma})_y = 0. \tag{2.1d}$$

Here, ρ is the density, p is the pressure, u and v are the x- and y-velocity components, respectively. The subscripts t, x or y indicate time or space derivatives.

2.2. *Self-similarity*

Since there is no characteristic length scale in the shock system, the problem has self-similar solutions which depend only on self-similar coordinates x/t, y/t where t is the time. The term pseudostationary coordinates is also used. Dimensionless self-similar coordinates (ξ, η) are defined by:

$$\xi = \frac{x}{Dt}, \quad \eta = \frac{y}{Dt} \quad \text{where} \quad D = \frac{D_i}{\cos\theta_w}. \tag{2.2}$$

In (ξ, η)-coordinates, the distance $L = |\mathrm{OE}|$ has unit length, where E is the intersection of the continuation of the i-shock with the ramp surface (figure 2).

The set of equations (2.1) for a self-similar flow reads:

$$(u-\xi D)\rho_\xi + (v-\eta D)\rho_\eta + \rho(u_\xi + v_\eta) = 0,$$
$$(u-\xi D)u_\xi + (v-\eta D)u_\eta + \rho^{-1}p_\xi = 0,$$
$$(u-\xi D)v_\xi + (v-\eta D)v_\eta + \rho^{-1}p_\eta = 0,$$
$$(u-\xi D)(p\rho^{-\gamma})_\xi + (v-\eta D)(p\rho^{-\gamma})_\eta = 0.$$

If $\boldsymbol{q} = (U, V)$ is the self-similar velocity vector with components

$$U = u - \frac{x}{t} = u - \xi D, \quad V = v - \frac{y}{t} = v - D\eta, \tag{2.3}$$

the set of equations can be written as

$$(\rho U)_\xi + (\rho V)_\eta + 2\rho D = 0, \tag{2.4a}$$
$$UU_\xi + VU_\eta + UD + \rho^{-1}p_\xi = 0, \tag{2.4b}$$
$$UV_\xi + VV_\eta + VD + \rho^{-1}p_\eta = 0, \tag{2.4c}$$
$$U(p\rho^{-\gamma})_\xi + V(p\rho^{-\gamma})_\eta = 0. \tag{2.4d}$$

Notice that the difference between the self-similar and the real velocity depends on the location. The additional velocity $(-\xi D, -\eta D)$ is the radial vector field centred at the origin O. Thus the flow is radial upstream of the i- and the n-shocks and is centred on O. The flow upstream of the r-shock is also radial, but centred on the tip of the vector $\boldsymbol{U}_i$. If the r- and the n-shocks are locally straight at the node, then locally the flow downstream of them is also radial and centred on the tips of the vectors $\boldsymbol{U}_r$ and $\boldsymbol{U}_n$, respectively. The tips of the vectors $\boldsymbol{U}_i$ and $\boldsymbol{U}_n$ are also centres for the radial flows near the node. These vectors are associated with the extended tangent to the contact discontinuity at the node (figure 2). The global convergence point for the flow downstream of the r- and n-shocks are, respectively, S and C (figure 2). Since $V = 0$, and U is continuous along the ramp surface, S is a stagnation point. For more details see Jones *et al.* (1951).

Finally, the self-similar Mach number is defined by:

$$M = \sqrt{\frac{U^2+V^2}{a^2}} \quad \text{where} \quad a^2 = \frac{\gamma p}{\rho}. \tag{2.5}$$

Hereinafter, unless otherwise stated, self-similar velocity and self-similar Mach number will be used.

3. The numerical method

We consider a plane incident shock in a perfect gas ($\gamma = \text{const}$), with Mach number $M_i = D_i/a_0$, diffracting over a ramp of angle θ_w. The unsteady flow is described by the conservation equations of mass, momentum and entropy (Euler equations). These equations were solved numerically using a W-modification of the Godunov method which has a second-order accuracy both in space and in time (for details see Vasilev 1996).

3.1. *The computational domain and the grid*

Curvilinear moving grids were used in the calculations. The initial position of the computational domain is shown in figure 3. The boundaries CT and TD were used to track the shock fronts during the calculations. The gas parameters behind the i-shock

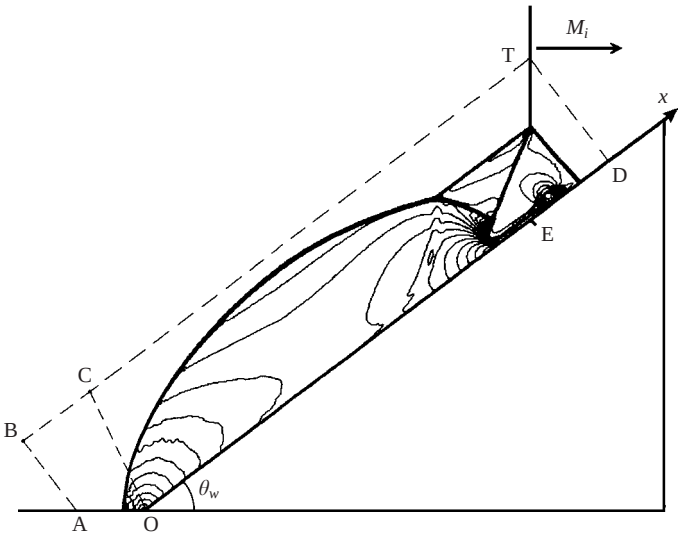

FIGURE 3. The boundaries of the moving computational domain. CT and TD are used for tracking the fronts of the *r*-, and *n*-shocks. M_i, the incident shock Mach number; θ_w, the ramp angle.

were set as the initial conditions for the entire domain. In order to reduce CPU-time, the results of the previous computation were employed as the initial condition for the following calculation in the production runs. The following boundary conditions were imposed:

(i) Zero normal velocity components along the ramp surface.
(ii) The parameters of the unperturbed gas at rest at the boundary TD.
(iii) The parameters of the gas behind the *i*-shock for all the other boundaries.

Since, as will be explained subsequently, a procedure for tracking the shock fronts was applied, the computational mesh became curvilinear. An example of the formed computational meshes for $M_i = 5$ and $\theta_w = 25°$ is shown in figure 4(*a*). In order to simplify the computational grid, the *r*-shock was only partially tracked, and its segment near O was located inside the computational domain, and thus, was smeared over 2–3 cells by a shock-capturing scheme. This segment was 10–30% of the length of the *r*-shock front.

A denser mesh was used near the node in order to improve the local accuracy of the computation (figure 4*a*). Four cells adjacent to the node were replaced by triangular cells with a common vertex T (see figure 4*b*). This simple procedure significantly increased the resolution of the contact discontinuity and the accuracy of the computations.

3.2. *Shock tracking*

The algorithm for the displacement of the mesh line and for tracking the shock front, is now described briefly. The scheme of the displacement of the jth node is shown in figure 5. For simplicity, it is assumed that the shock propagates to the right into a quiescent gas. Let the point S_j^n be the common point of the adjacent $(j-1)$th and jth segments of the shock front at time t_n. It is required to determine the displacement of the point S_j^n along the given directrix L_j during the time interval Δt to its new position S_j^{n+1}.

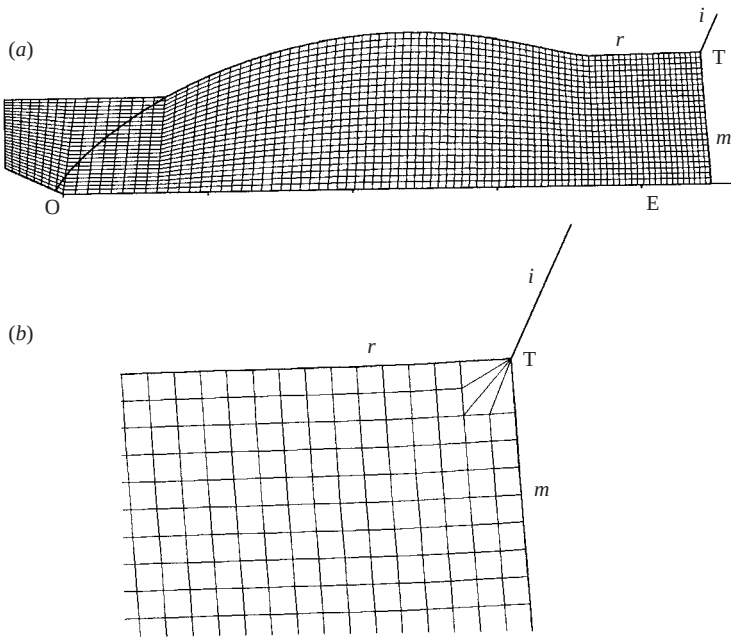

FIGURE 4. (*a*) An example of the formed computational mesh (only every fifth mesh-line is plotted) for a typical case. (*b*) The structure of the computational grid near the node.

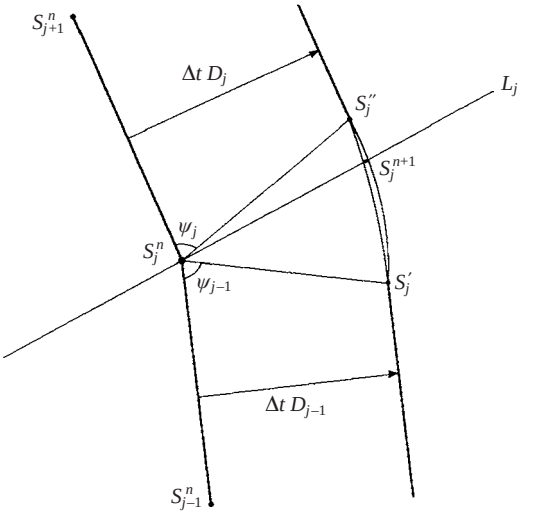

FIGURE 5. The modified scheme for calculating the motion of the shock node, while accounting for the propagation of the perturbations behind the shock front.

The displacement velocities D_{j-1} and D_j of the segments $S_{j-1}^n S_j^n$ and $S_j^n S_{j+1}^n$ in a direction normal to them are found by solving the Riemann problems with the initial parameters of the cells located on the two sides of these segments. The disturbances propagating from point S_j^n follow the straight segments of the shock front and deform it into a curvilinear segment $S_j' S_j''$. The position of the curvilinear segment can be

determined using an acoustic approximation:

$$\tan^2 \psi_j = \frac{(\gamma+1)M_j^4}{\left(M_j^2-1\right)\left[2+(\gamma-1)M_j^2\right]}, \tag{3.1}$$

where M_j is the Mach number of the jth segment of the shock front. A similar procedure is employed for the $(j-1)$th segment. If the directrix L_j does not intersect the curvilinear segment $S_j'S_j''$, then the new position S_j^{n+1} is determined as the point of intersection of the directrix L_j with one of the straight segments. In the case of two intersections, the one that is further away from the S_j^n point is selected. Otherwise, S_j^{n+1} is determined by the average between the points of intersection of the directrix L_j with the two circles that pass through S_j' and S_j'' and the tangent to one of the straight segments (figure 5). This procedure can be easily generalized to the case of a moving directrix L_j and to inhomogeneous flow ahead of the shock.

In the calculations of the motion of the node in an MR system, the directrix is the i-shock front, and the curvilinear segment is replaced by continuing the straight segments of the wave.

The algorithm differs from similar algorithms in that we perform smoothing of the front using a physical mechanism, namely the propagation of disturbances behind the shock front. Its high efficiency is demonstrated by the successful calculation of weak shock reflections under the conditions of the von Neumann paradox (Vasilev 1999).

If the grid line does not coincide with the front of the tracked wave (e.g. at the initial moment), then the mesh line moves as a weak disturbance when the solution of the Riemann problem is employed. Eventually, it does coincide with a wavefront because the upstream perturbation velocity is smaller than the front velocity, whereas the downstream perturbation velocity is larger than that of the front. Thus, the algorithm simultaneously solves two problems, namely, shock capturing and shock tracking.

After each time step the length OE (figure 3) is used to normalize the coordinates of the mesh points. Thus, once the solution attains a self-similar state, the mesh and all the flow parameters become constant. The calculations were performed until the solution attained this state. Both the absolute value of the time derivative of the density and that of the trajectory angle of the node were used as quantitative estimates of the degree of unsteadiness (Vasilev 1998). The calculations showed that the latter estimate was the most robust, since the node trajectory angle was the slowest to attain the self-similar state. Note that the renormalization of the mesh coordinates at each time step is performed only for convenience and does not affect the results of calculations.

In all the cases where the jets were stable (§4.7), the self-similar state was attained with high accuracy. When the jet was unstable, the calculation times were extended two to three times as compared to those with stable jets.

4. Numerical and analytical results

4.1. *The wave systems*

Forty-eight calculations were done for all the combinations of the i-shock Mach numbers: $M_i = 1.5, 2, 2.5, 3, 4, 5$ and ramp angles: $\theta_w = 5^\circ, 10^\circ, 15^\circ, 20^\circ, 25^\circ, 30^\circ, 35^\circ, 40^\circ$. A compendium of the results (constant density contours), in the vicinity of the node, is shown in figure 6. Hereinafter, unless otherwise stated, the specific heat ratio is $\gamma = 1.4$. The angles of the shocks in the vicinity of the node could be determined

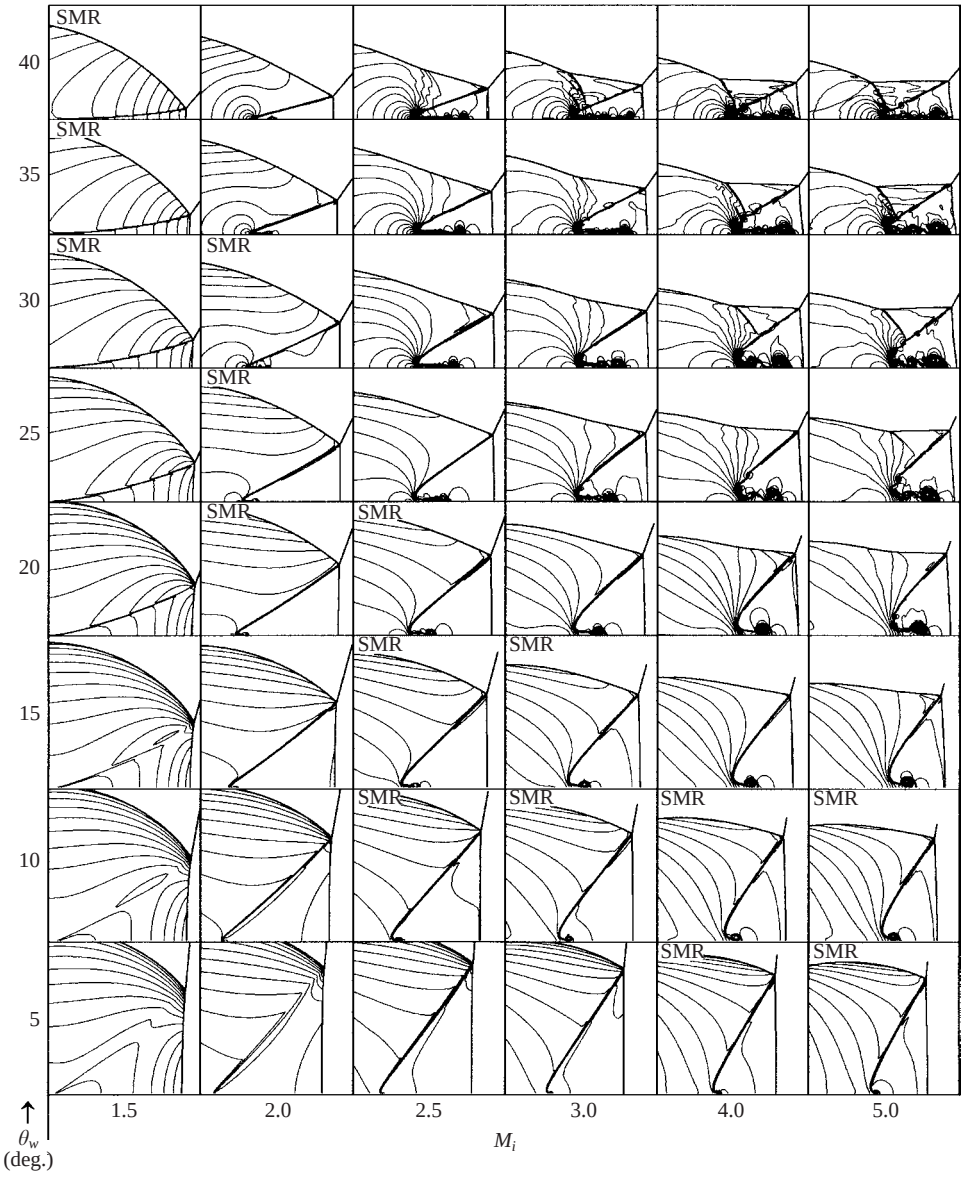

FIGURE 6. Wave systems for $\gamma = 1.4$. The ramp angle, θ_w, varies from 5° to 40°, the i-shock Mach number, M_i, varies from 1.5 to 5. The single-Mach reflection systems are labelled SMR.

with high accuracy by employing the front tracking technique. This enabled us the use of the three-shock theory to classify the various types of wave configuration. Distinct single-Mach reflection (SMR) configurations are indicated in figure 6.

The two-node reflection (also called a double-irregular reflection (DIR), §4.3) domain extends to the upper right of the SMR-domain. There is a transitional domain between the SMR and DIR domains. In a transitional-irregular reflection (TIR), the second node spreads out into a convex bend along the r-shock; see for example the system for $M_i = 3$, $\theta_w = 30°$. Following Olim & Dewey (1992) the

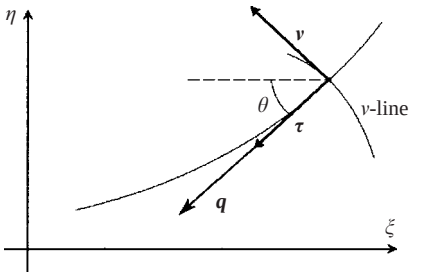

FIGURE 7. The curvilinear coordinates (τ, ν).

weak-Mach reflection (WMR) and von Neumann reflection (vNR) domains extend to the lower left of the SMR-domain.

Jetting clearly exists for all the TIR and DIR configurations. Moreover, the calculations qualitatively agree with experiments in that the jet curves upstream along the ramp surface, rolls up behind the n-shock, and drives this shock further forward as the value of M_i increases. Jetting is also found in the SMR, WMR and vNR systems with $M_i \geqslant 2$, although it is not so pronounced. The results show no-jetting for all the cases with $M_i = 1.5$. Thus, it may be concluded that there is no direct correlation between the appearance of the jet and a particular type of shock system.

4.2. *Analytical model for jetting ↔ no-jetting transition*

We apply (2.4) to the flow region under the contact discontinuity. It is assumed that the flow has a locally radial velocity field behind the n-shock. We use the hodograph variables (q, θ) where:

$$q = \sqrt{U^2 + V^2}, \quad U = -q\cos\theta, \quad V = -q\sin\theta. \tag{4.1}$$

We also use orthogonal curvilinear coordinates (τ, ν) attached to the streamlines, such that the ν-lines (i.e. the curves for which $\tau = \text{const}$) are orthogonal to the τ-lines (figure 7).

Equation (2.4a) becomes

$$\rho\frac{\partial q}{\partial \tau} + q\frac{\partial \rho}{\partial \tau} - \rho q\frac{\partial \theta}{\partial \nu} + 2\rho D = 0, \tag{4.2}$$

whereas (2.4b) and (2.4c) yield an equation with derivatives along the streamline:

$$\rho q\frac{\partial q}{\partial \tau} + a^2\frac{\partial \rho}{\partial \tau} + \rho q D = 0, \tag{4.3}$$

where a is the speed of sound. The $\partial\theta/\partial\nu$ derivative measures the curvature of the ν-line and the narrowing of a stream tube, about the streamline. Eliminating the density from (4.2) and (4.3) we obtain,

$$q\frac{\partial \theta}{\partial \nu} = (1 - M^2)\frac{\partial q}{\partial \tau} + (2 - M^2)D, \tag{4.4}$$

where $M = q/a$ is the Mach number.

Consider the no-jetting case for which the contact discontinuity ends at C on the wall (figure 8). The velocity field is radial upstream of the n-shock (see § 2.2), but it is

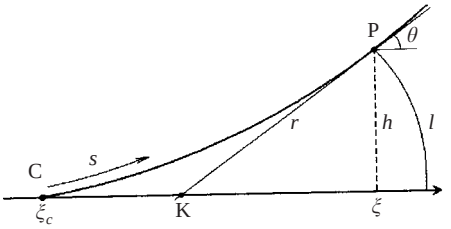

FIGURE 8. Geometry for a radial velocity field below the contact discontinuity.

radial downstream of it only for straight shocks. Nevertheless, it will be assumed that all the flow field under the contact discontinuity is locally radial, so $\theta(\tau, \nu)$ depends linearly on ν. Consequently, for a fixed τ we have

$$\frac{\partial\theta}{\partial\nu} = \text{const} = \frac{1}{r},$$

i.e. the ν-contours are arcs with radius r. Figure 8 shows an arc of length l, passing through an arbitrary point P on the contact discontinuity. The radius of the arc is equal to the segment PK, which is tangent to the contact discontinuity at P. Since r may change along the streamline it can depend on ξ.

The curvilinear length of the contact discontinuity measured from C is denoted by s. Applying (4.4) to the streamline along the lower side of the contact discontinuity yields

$$\frac{q}{r(s)} = (2 - M^2)D - (1 - M^2)\frac{\mathrm{d}q}{\mathrm{d}s}. \tag{4.5}$$

Let $h(s)$ be the distance from P to the ramp surface along the normal to the ramp, then (4.5) can be written as:

$$\frac{q}{h}\frac{\mathrm{d}h}{\mathrm{d}s} = (2 - M^2)D - (1 - M^2)\frac{\mathrm{d}q}{\mathrm{d}s}. \tag{4.6}$$

Applying (4.6) to a small neighbourhood around C, where $M \approx 0$, we obtain a simple differential equation, linking the shape of the contact discontinuity $h(s)$ with the velocity $q(s)$:

$$\frac{1}{h}\frac{\mathrm{d}h}{\mathrm{d}s} + \frac{1}{q}\frac{\mathrm{d}q}{\mathrm{d}s} = \frac{2D}{q}. \tag{4.7}$$

Let us assume that the particle velocity along the contact discontinuity and under it, approaches zero near C according to a power law $q(s) = ks^\beta$. The general solution $h(s)$ to (4.7) is:

$$q = ks^\beta \Rightarrow \begin{cases} h(s) = \dfrac{1}{ks^\beta}\exp\left(\dfrac{2D}{k(1-\beta)}s^{1-\beta}\right) & \text{if} \quad \beta \neq 1, \\ h(s) = \dfrac{1}{k}s^{2(D/k)-1} & \text{if} \quad \beta = 1, \end{cases} \tag{4.8}$$

Three cases of (4.8) must be considered:

Case 1: $\beta < 1$. This case has no physical meaning, because the initial condition, $h(0) = 0$, is not satisfied.

Case 2: $\beta > 1$. The contact discontinuity merges smoothly into the ramp surface, and all the derivatives of $h(s)$ vanish at C. The theory yields no conditions for the onset of jetting in this case.

Case 3: $\beta = 1$. The power relation for $h(s)$ has the exponent

$$\lambda = 2\frac{D}{k} - 1.$$

If $\lambda < 2$, the contact discontinuity curvature becomes infinite at C. This singularity should produce an increase in the pressure along the streamline at the upper side of the contact discontinuity, thereby causing the onset of the jetting effect. Thus, the effect appears only if,

$$\lambda = \frac{2D}{k} - 1 < 2 \quad \text{where} \quad k = \left.\frac{\mathrm{d}q}{\mathrm{d}s}\right|_C. \tag{4.9}$$

The criterion (4.9) has a simple geometrical interpretation. The calculations show that when jetting occurs, the $q(s)$ dependence is nearly linear between C and the node, i.e. $q = ks$. This allows us to associate the criterion (4.9) with the characteristics of the node. We apply (4.5) to a neighbourhood of the node

$$q_3\frac{1}{r_m} = \left(2 - M_3^2\right)D - k\left(1 - M_3^2\right),$$

where r_m is the tangent segment to the contact discontinuity at the node before it intersects the ramp surface; q_3 and M_3 are the velocity and the Mach number behind the n-shock at the node. Since $q_3 = ks_m$, where s_m is the full length of the contact discontinuity from the node to C, we obtain

$$\frac{s_m}{r_m} = \lambda - \tfrac{1}{2}(\lambda - 1)M_3^2 \quad \text{where} \quad \lambda = 2\frac{D}{k} - 1.$$

Thus, the criterion (4.9) has the following interpretation,

$$\lambda < 2 \Leftrightarrow \frac{s_m}{r_m} < 2 - \tfrac{1}{2}M_3^2, \tag{4.10}$$

that is, when jetting appears, the ratio of the length of the contact discontinuity to the length of the tangent segment does not exceed $2 - 0.5M_3^2$. Jetting occurs only if the condition given by (4.10) is satisfied. However, this condition is not sufficient, if for example $\beta > 1$ in (4.8), then jetting may not occur. Noting that the Mach number M_3 cannot exceed 1, it is possible to obtain a simple approximate criterion for jetting,

$$s_m < \tfrac{3}{2}r_m. \tag{4.11}$$

Using (4.6) and the linear dependence $q = ks$, a relation for the shape of the contact discontinuity can be obtained by assuming that the sound speed variations are small enough to be neglected:

$$q = ks, \quad M = \frac{ks}{a}, \quad a = \text{const} = a_3.$$

Then,

$$\frac{1}{h}\frac{\mathrm{d}h}{\mathrm{d}s} = \frac{\lambda}{s} - s\mu,$$

	$M_i = 1.6$	$M_i = 1.7$	$M_i = 1.8$
s_m/r_m	1.81	1.56	1.29
$2-0.5\,M_3^2$	1.78	1.80	1.82
Criterion (4.10)	No-jetting	Jetting	Jetting
Computation	No-jetting	No-jetting	Jetting

TABLE 1. Numerical validation of the jetting $\leftrightarrow$ no-jetting criterion given by (4.10), for $\gamma = 1.4$, $\theta_w = 30^\circ$ and three different i-shock Mach numbers.

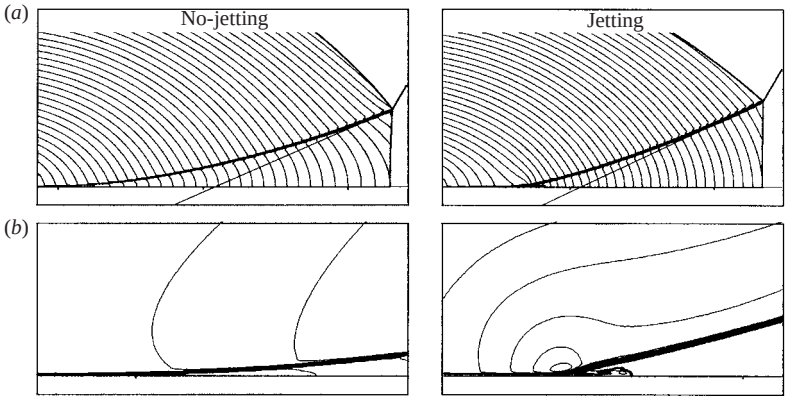

FIGURE 9. (a) Flow Mach number contours ($\Delta M = 0.02$) for $\theta_w = 30^\circ$, $M_i = 1.6$ (left) and $M_i = 1.8$ (right), $s_m/r_m = 1.81$ (left) and 1.29 (right). (b) Density contours ($\Delta\rho/\rho_0 = 0.02$) for fragments of the flow field near the point where the contact discontinuity merges with the ramp surface, zoom in factor four.

where

$$\lambda = \frac{2D}{k} - 1, \quad \mu = \frac{k(D-k)}{a_3^2} = \tfrac{1}{2}(\lambda - 1)\tfrac{M_3^2}{s_m^2}.$$

The solution for $h(s)$ is

$$h(s) = C \cdot s^{\lambda} \exp\left(-\mu\left(\tfrac{1}{2}s^2\right)\right).$$

The constant C is found from the condition $h(s_m) = h_m$.

The criterion (4.10) was validated numerically for three cases $\gamma = 1.4$, $\theta_w = 30^\circ$ and $M_i = 1.6$, 1.7 and 1.8. Adaptive mesh refinement was used with a grid of 1500×500. The results are presented in table 1. It can be seen that the prediction of the criterion is incorrect only for $M_i = 1.7$. The latter, supports the remark that the criterion is necessary, but not sufficient, for the prediction of the onset of the effect.

Figure 9 shows Mach number and density contours for the flow fields of the extreme cases, $M_i = 1.6$ and $M_i = 1.8$, presented in table 1. The wave configuration and the discretization of the Mach number contours show that the flow under the contact discontinuity is locally nearly radial. Since the jet is very small, the absence of jetting in the computations, for the intermediate case, $M_i = 1.7$, can be explained by insufficient resolution of the numerical simulation.

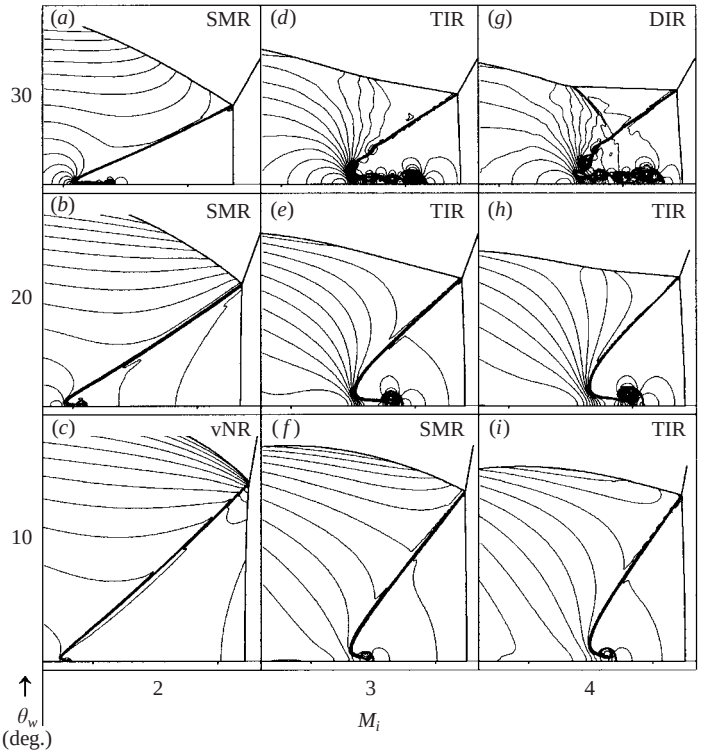

FIGURE 10. Enlargement of 9 of the 48 cases shown in figure 6 illustrating the jetting for different combinations of M_i and θ_w. SMR, single-Mach-reflection; *TIR*, transitional-irregular-reflection; *DIR*, double-irregular-reflection; *vNR*, von Neumann-reflection.

4.3. *The jetting configurations*

Nine scaled-up systems for all the combinations with $M_i = 2$, 3 and 4 and $\theta_w = 10°$, 20° and 30° are shown in figure 10. The systems comprise different irregular reflections, namely, *vNR*, SMR, *TIR* and *DIR*. All the calculations reveal a curving of the slipstream towards the Mach stem near the ramp surface, and the formation of a jet that drives towards the foot of the *n*-shock. However, the size of the jets and the flow patterns associated with them vary considerably. When the angle between the contact discontinuity and the ramp surface is large, the jet is rather short, i.e. its length and width are of the same order (figure 10*f*, *i*). When the angle decreases, the length of the jet increases and becomes much larger than its width (figure 10*a*, *d*, *g*). Kelvin–Helmholtz instabilities develop along the jet, and along the adjacent part of the contact discontinuity (figure 10*d*, *g*). As will be shown subsequently, non-periodic vortical perturbations in the jet were detected in the calculations when mesh refinement was applied.

In the case of no-jetting SMR, the *n*-shock is either concave or nearly plane (figure 6). However, when jetting does occur, part of the *n*-shock is driven forward and becomes locally convex forward. More precisely, an inflection point develops on it, causing it to be convex below the inflection, and concave above it. Four examples are shown in figure 11 for constant values of γ and M_i and different values of θ_w, and another four in figure 12 for a fixed values of θ_w and different values of γ and M_i. There are DIR configurations in figures 11(*a*), 12(*a*) and 12(*b*), and TIR in

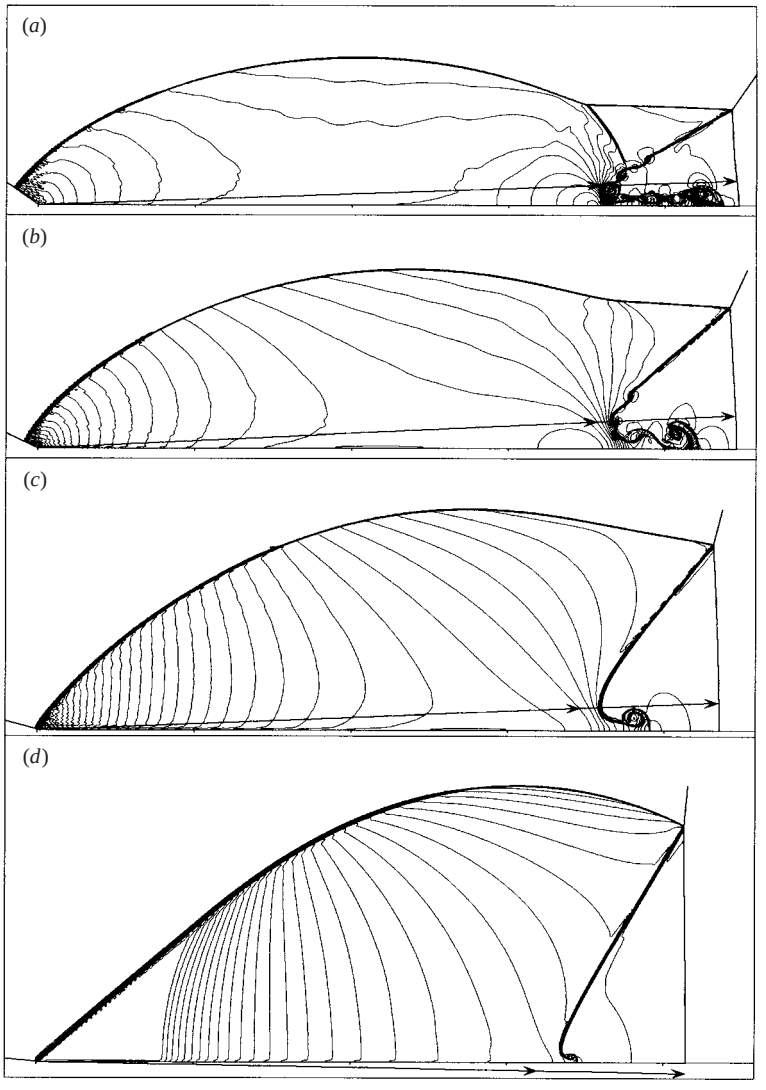

FIGURE 11. Density contours for $M_i = 4$. (*a*) $\Delta\rho/\rho_0 = 0.248$, $\theta_w = 35°$; (*b*) 0.162, 25; (*c*) 0.08, 15°; (*d*) 0.026, 5°. The arrowed lines are parallel to the velocity vectors of the *n*-shocks at their respective nodes.

figures 11(*b*), 11(*c*) and 12(*c*). The convex/concave shape is clearly visible in the DIR, but is less pronounced in the TIR. The $\boldsymbol{D}_n$ and $\boldsymbol{U}_n$ vectors are above the ramp surface for all these flows. By contrast, the vectors are below the surface in figures 11(*d*) and 12(*d*), and the *n*-shocks are virtually plane for these cases. In the special case when $\boldsymbol{D}_n$ and $\boldsymbol{U}_n$ coincide with the surface ($\boldsymbol{D}_n = \boldsymbol{D}_m$ and $\boldsymbol{U}_n = \boldsymbol{U}_m$), the *n*-shock is everywhere plane and normal to it. For self-similar coordinates, the flow approaches the *n*-shock radially, so even when this shock is everywhere normal to the surface, it is nevertheless an oblique shock everywhere except at the surface where it is locally a normal shock.

When the $\boldsymbol{D}_n$ and $\boldsymbol{U}_n$ vectors are above the surface, the angular width of the jet is confined between them and the surface. Consequently, the angle between the $\boldsymbol{D}_n$

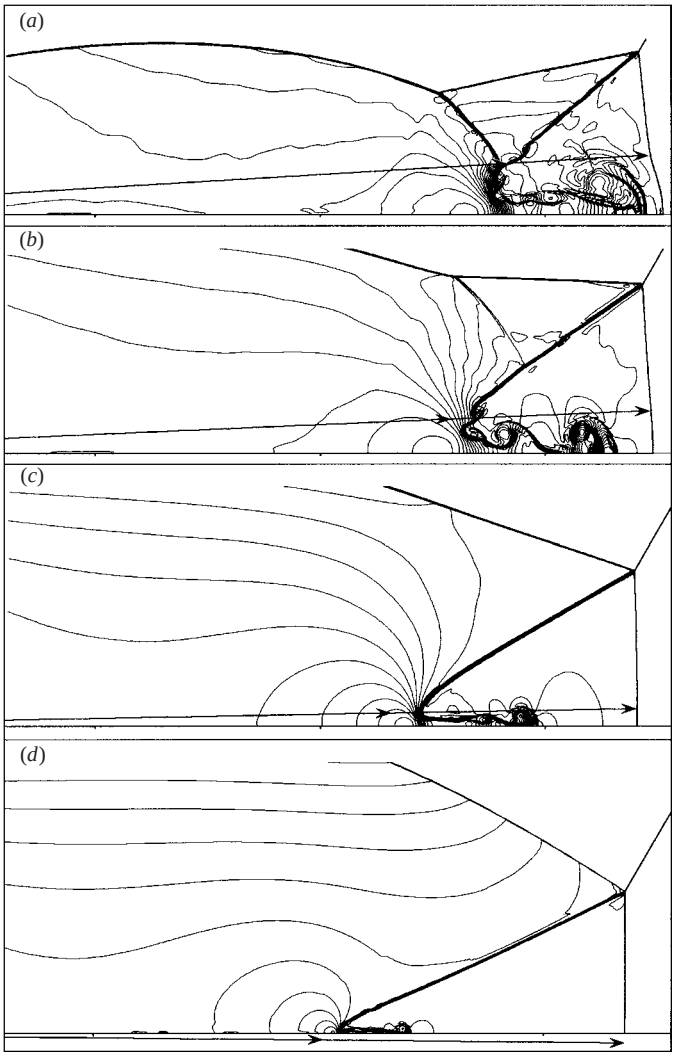

FIGURE 12. Density contours for $\theta_w = 30°$. (*a*) $M_i = 7$, $\gamma = 1.3$, $\Delta\rho/\rho_0 = 0.45$, (*b*) 4, 1.4, 0.2; (*c*) 2.5, 1.4, 0.075; (*d*) 2, 1.4, 2.

and $\boldsymbol{U}_n$ vectors and the surface is an approximate measure of the angular width of the jet. Thus, the width of a jet is determined by the angle of the *n*-shock at the node. Furthermore, the tip of $\boldsymbol{U}_n$ is close to the point where the jet turns towards the node. In figures 11(*d*) and 12(*d*), which are SMR systems, the jet is small, and the dependence disappears.

The DIR for $M_i = 7$ in figure 12(*a*) is, in fact, a 'negative' DIR, i.e. the second node trajectory angle is smaller than that of the first one (for details see Ben-Dor 1991). As will be shown subsequently, in this particular case and for cases with smaller values of M_i, the jet is unstable. Well-defined vortex structures are formed along the contact discontinuity, and move towards the boundary of the jet. The characteristic size of these structures is less than the width of the jet, consequently it is the jet boundary which is mainly subject to the perturbations. The vortex at the end of the jet is large, and causes strong deformation of the foot of the *n*-shock. Local shocks appear inside

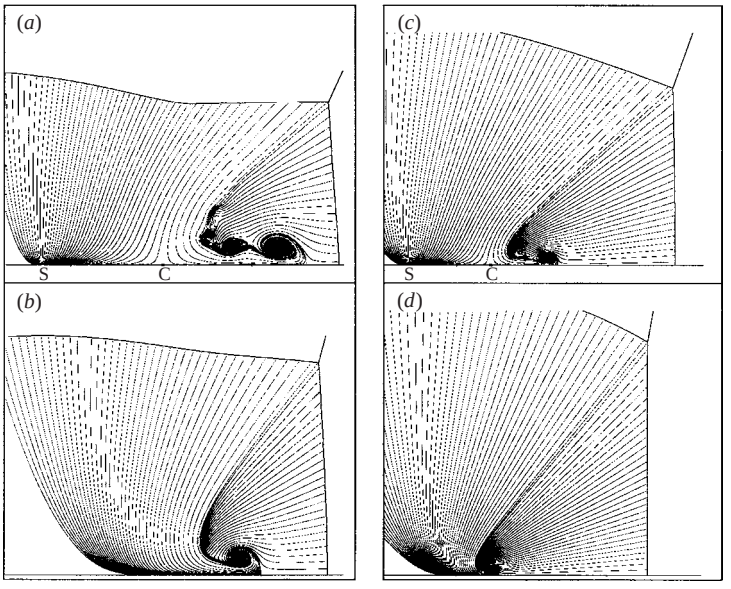

FIGURE 13. Streamlines of the self-similar velocity field. C, a normal impact/stagnation point; S, a stagnation point. A slug whose length is CS exists in cases (*a*) and (*c*). There is no slug in cases (*b*) and (*d*). All the streamlines passing through the *i*–*r* sequence enter the jet. (*a*) $M_i = 5$, $\gamma = 1.4$, $\theta_w = 25°$; (*b*) 5, 1.4, 15°; (*c*) 4, 1.67, 20°; (*d*) 4, 1.67, 10°.

the vortex near the ramp surface and at its periphery. Their positions are unstable because of the jet pulsation.

4.4. *The stagnation points*

Streamlines of the self-similar velocity field are shown for four cases in figure 13 for $\gamma = 1.4$ and 1.67. Consider the streamlines passing through the *i*–*r* sequence. In figure 13(*a*), there is a particular streamline that makes a normal impact on the ramp surface at C, this is a stagnation point. The streamlines between that one, and the one passing through the node comprise the jet. Since the streamlines split at C, it is also a branch point. The rest of the streamlines pass downstream and terminate at the other stagnation point S.

Those streamlines, which approach S from the right, comprise the slug whose length is CS. Other streamlines approach S from the left and also terminate there. They comprise the flow that drives the TIR configuration to the right. The streamlines passing through the *n*-shock simply spiral around the vortices formed by the jet. A Kelvin–Helmholtz instability is visible at the jet boundary in figure 13(*a*). Note that in this case the flow in the jet is not steady and the instantaneous streamlines of the velocity vector field may differ from the streamlines of the particles. Neither of the stagnation points C or S are present in figures 13(*b*). It appears as if they have merged together and proceeded to the front of the jet. All the streamlines that pass through the *i*–*r* sequence, and the *n*-shock comprise the jet. They all terminate at $t = \infty$ at the centre of the vortex. As shown in figures 13(*c*) and 13(*d*), similar behaviour is also observed for $\gamma = 1.67$, but here the branch point C appears for a smaller value of θ_w. The existence of C is not associated with any particular type of reflection. However, as will be shown subsequently, C indicates that the jetting is strong and the

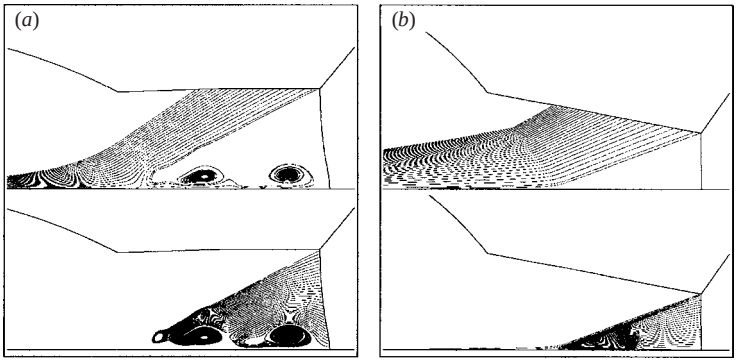

FIGURE 14. Streamlines in strong and weak jetting for $M_i = 5$: (*a*) strong jetting for $\theta_w = 40°$; (*b*) weak jetting for $\theta_w = 55°.15$

jet unstable. The local increase of the pressure at such a point results in an increase of the length of the jet.

4.5. *Strong and weak jetting*

If the ramp angle is increased to about 40° the flow remains similar to that shown for $\theta_w = 25°$ in figure 13(*a*). Streamlines calculated for $M_i = 5$, $\theta_w = 40°$ and $\gamma = 1.4$ are presented in figure 14(*a*). The upper part of the figure shows streamlines that have pass through the *i*–*r* sequence, but only a small fraction of them are part of the jet. The streamlines that pass through the *n*-shock are in the lower part of the figure. Unexpectedly, they also turn upstream to join the jet. This is possible because the *n*-shock is curved, and the entropy is generally less than that of a normal shock on the ramp surface. The flow behind the weaker part of the *n*-shock has more kinetic energy and momentum. However, even in the latter case it has less kinetic energy and momentum than the flow through the *i*–*r* sequence. When the jet comprises part of the flow passing through the *i*–*r* sequence and that passing through the *n*-shock, the jetting is defined to be strong jetting. The strong jetting shown in figure 14(*a*) drives the foot of the *n*-shock forward.

As can be seen in figure 14(*b*), the flow pattern changes from jetting to no-jetting if the ramp angle is increased to $\theta_w = 55°$. All the streamlines through the *i*–*r* sequence now pass into the slug flow. Remarkably, a jet still exists in the *n*-shock flow with a vortex at its front. This jet is formed from the streamlines close to the node where the entropy is less than that at the foot of the *n*-shock. This jet has less kinetic energy than the jet in the strong case, so we define it as weak jetting.

4.6. *Near detachment* ($\theta_w \rightarrow \theta_e$) *wave systems*

Any irregular reflection (IR) will eventually change to a regular reflection (RR) if the ramp angle is increased sufficiently. Shock tube experiments show that the RR $\leftrightarrow$ IR transition occurs at the detachment criterion $\theta_w = \theta_e$. Similarly, transition from strong to weak jetting is also accompanied by changes in the wave configuration. Results of calculations for the four combinations of $M_i = 5$, $\gamma = 1.4$ and $\theta_w = 45°$, 50°, 55° and 58° are shown in figure 15 (the subsonic flow regions are shaded for 50°, 55° and 58°). Large perturbations are seen in the contours associated with the contact discontinuity and the jet for $\theta_w = 45°$ (figure 15*a*). The perturbations are negligible for $\theta_w \geqslant 50°$. For $\theta_w = 58°$, the jet is so thin that it nearly vanishes. The systems for $\theta_w = 50°$,

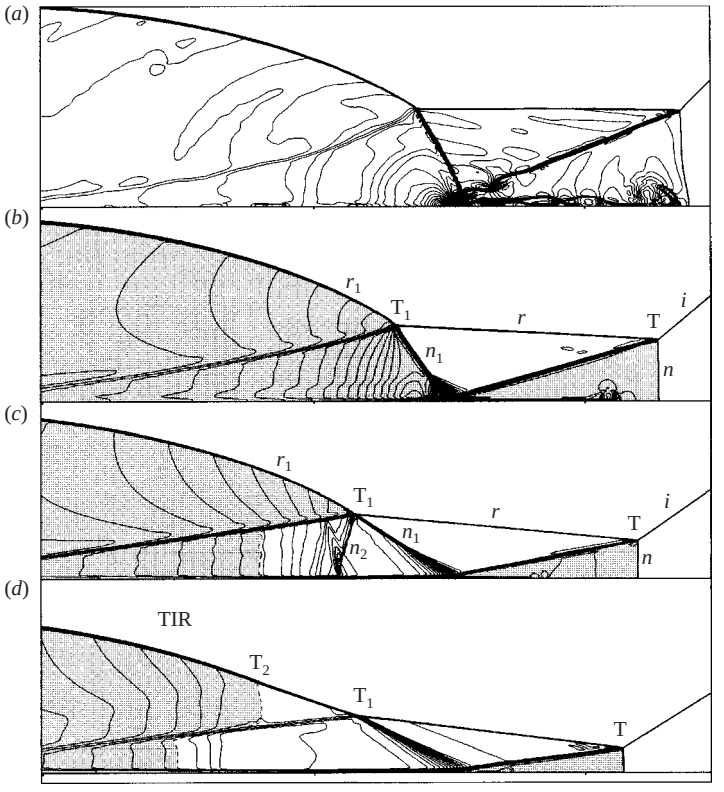

FIGURE 15. Density contours for some large ramp angles with $\gamma = 1.4$, $M_i = 5$. For (*a*) $\theta_w = 45°$; (*b*) 50°; (*c*) 55°; (*d*) 58°. The subsonic regions are shaded in frames (*b*), (*c*) and (*d*). T is a Mach node for all for cases; T_1 is a degenerate overtaking node in (*a*), (*b*), but it is a (non-degenerate) overtaking node in (*c*), (*d*) see also the refinement in figure 16.

55° and 58° are in the dual-solution domain, where both regular (RR) and irregular (SMR, TIR or DIR) reflections are theoretically possible. Experiments in diatomic gases with $M_i \approx 5$ show RR in this domain, whereas the numerical simulations yield irregular reflections (figure 15*b–d*). A boundary layer which is always present in ramp experiments is not accounted for in the present Euler calculations. Calculations using the Navier–Stokes equations, which simulated a laminar heat-conducting boundary layer (Henderson *et al.* 1997, 2001) showed that both regular and irregular reflections can occur in the dual-solution domain. The simulations also showed that the boundary layer made it possible for the regular reflection to persist into the IR-domain. However, this persisted-regular-reflection (PRR) was dynamically unstable, and after a time it changed suddenly into an irregular reflection, and then rapidly evolved into a self-similar system. Near $\theta_w \to \theta_e$, the persistence of RR increases to the extent that it exceeds the observation times available for the experiments, as has happened in many experimental investigations. However, by using large enough shock-tube test sections (i.e. long enough ramp surfaces) Dewey & van Netten (1991, 1995) succeeded in detecting the earlier regular wave configuration becoming irregular, and Henderson *et al.* (2001) were able to photograph the evolution of these wave patterns during experiments. By contrast, there is no boundary layer and thus no PRR for the Euler calculations, so the irregular system appears immediately.

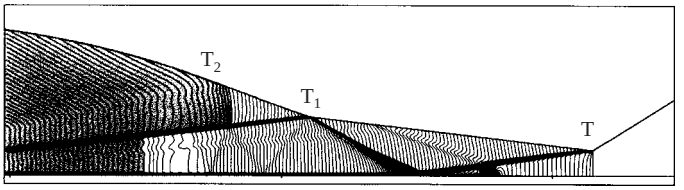

FIGURE 16. Self-similar Mach number contours for the case shown in figure 15(*d*) as calculated using a mesh refinement with a weak shocks emanating from T_1.

The way that information flows into and out of the nodes T and T_1 can be used to classify wave systems in figure 15 following Glimm *et al.* (1985). If the particle velocity vector is resolved into vectors parallel and perpendicular to a wave or a contact discontinuity (CD) then the information flows in the same direction as the parallel vector. In figure 15, T is a Mach node everywhere because the *i*-shock arrives at T, while the CD, the *r*- and *n*-shocks all leave it (see also figure 6*a* in Henderson & Menikof 1998). In figure 15(*b*), the *r* and n_1-waves arrive at T_1 while the r_1-shock and the CD leave it. Furthermore, the *r*- and n_1-shocks are in the same family, which implies that T_1 is an overtaking node (Glimm *et al.* 1985; see also figure 6*c* in Henderson & Menikoff 1998). Notice that the flow downstream of the n_1-shock is subsonic. By contrast, the flow downstream of the n_1-shock is supersonic in figure 15(*c*), and a fourth wave n_2 can propagate from T_1. By definition the T_1 node in figure 15(*c*) is an overtaking node (see figure 6*d* in Henderson & Menikoff 1998), but because the n_2-wave is missing in figures 15(*a*) and 15(*b*), T_1 is a degenerate overtaking node in these cases (see figure 6*c* in Henderson & Menikoff 1998).

The flow behind the *r*- and *n*-shocks impacts on the ramp, as evidenced by the direction of the CD from T. These flows must curve to satisfy the boundary conditions. The subsonic path behind the *n*-shock enables these conditions to be communicated to the flow. The curvature of the contact discontinuity near the surface generates the fan that converges to the n_1-shock in figures 15(*b*) to 15(*d*). The impact also generates a shock which is like a bow shock detaching from a blunt body (the ramp is the blunt body). As it detaches, the bow shock interacts with the *r*-shock and the contact discontinuity from T to produce T_1, and its associated waves r_1, n_1 and the second contact discontinuity (figure 15*a–c*). The r_1–n_1 shock combination can be thought of as the bow shock after it has interacted with the *r*-shock and the second contact discontinuity. There is a subsonic path behind the bow shock between T_1 and the ramp. By contrast, the flow is everywhere supersonic behind the T_1 node in figure 15(*d*), so it is generated entirely by disturbances arising upstream of it. A more refined calculation, resolves a very weak outgoing wave, n_2, emanating from T_1; so T_1 is an overtaking node (figure 16). The contours are for self-similar Mach number with a small increment of 0.01. The n_2-wave reflects off the ramp and refracts through the second contact discontinuity producing a weak bend at T_2. The flow passes through a sonic surface behind the refracted wave, and behind the final reflection from the ramp (figures 15 and 16). The sonic surfaces are like corner signals, and are similar to the corner signals found in the Navier–Stokes calculations of Henderson *et al.* (1997).

In summary, for all the two-node DIR systems in figure 15, there is a Mach node at T and an overtaking node at T_1, but the T_1 node is degenerate in figures 15(*a*) and 15(*b*), because the n_2-shock is absent. The wave systems in figures 15(*a*) and 15(*b*) were previously called double-Mach reflections (DMR), but the name is now seen to

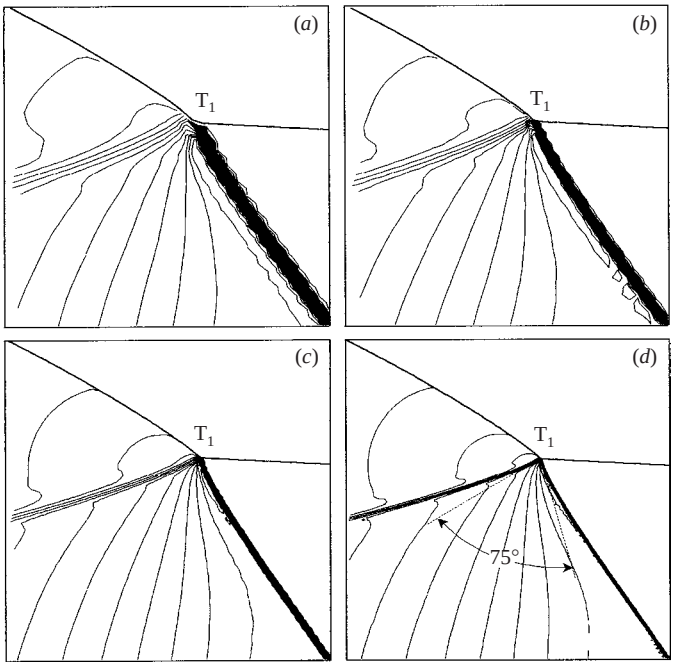

FIGURE 17. Isopycnics near the second node T_1, for the case shown in figure 15(b) calculated on different grids. (a) 400×50 grid; (b), (c) and (d) mesh refinement by a factor of 2 between the successive grids. The density contour increment is $\Delta\rho/\rho_0 = 0.3$.

be misleading because each system has only one Mach node. Furthermore, because of the bend at T_2, the system in figure 15(d) was called a transitional-double-Mach-reflection (TDMR), but as it also has only one Mach node it has been renamed here a transitional-double irregular-reflection (TIR).

The T_1 overtake node in figure 15(b) is now examined in more detail. Using its calculated coordinates, the self-similar Mach number ahead of it is $M = 2.2$, and the angle of incidence of the on-coming flow 47°. Applying the familiar three-shock (von Neumann) theory for a Mach node to this data gives the angle $56.4° < 90°$ between the n_1-shock and the contact discontinuity from T_1. This, of course, differs from the overtake node result in figure 15(b) where the angle is greater than 90°. However, it is possible to obtain a Mach node at T_1 for the system in figure 15(b), by refining the calculations for the flow near the node. In figure 17, there are four meshes with a refinement factor of 2 between the successive grids; figure 17(a) corresponds to the grid used in figure 15(b) whereas figure 17(d) corresponds to a Mach node. The refinements clearly show curvature of the fronts near T_1. However, the refined angle is $75° < 90°$ in figure 17(d); it is still significantly greater than the result from the three-shock theory (56.4°). A possible explanation is a lack of resolution even on the finest grid, which would imply that the domain where the fronts are strongly curved is very small. More accurate results or a better agreement could be obtained by using adaptive front tracking of all the wavefronts at the node T_1 (for details see Vasilev 1999).

The angle (β_1) between the CD and the n_1 shock is greater than 90° in figure 15(b), but less than 90° in figure 17(a). So the transition condition between the two nodes is where n_1 is a normal shock, $\beta_1 = 90°$. We note that Colella & Henderson (1990)

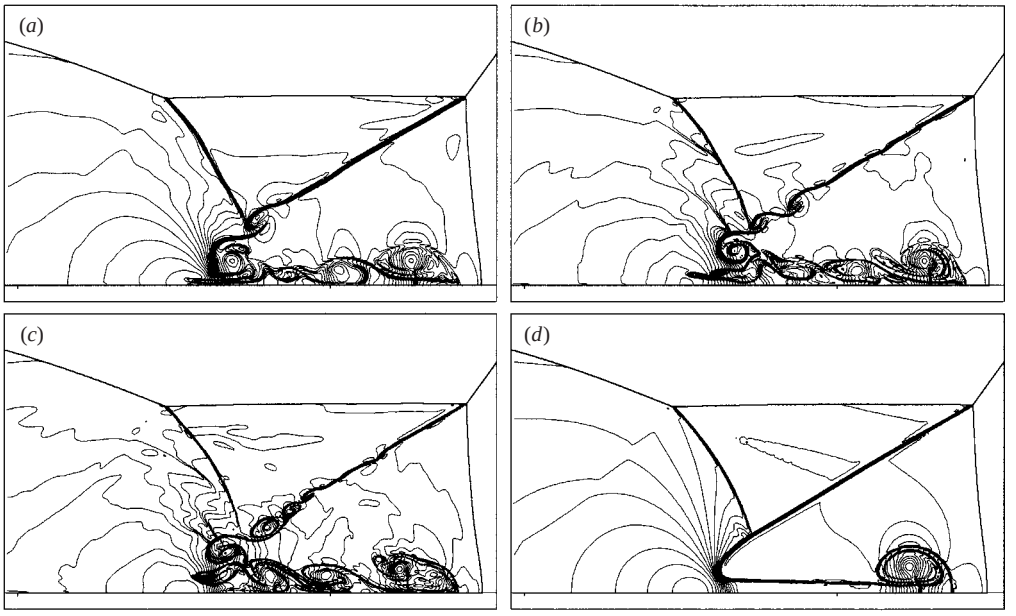

FIGURE 18. Calculations of an unstable jet on different grids, with $M_i = 4.5$ and $\theta_w = 36°$. (*a*) a 400×100 grid; (*b*) a 600×150 grid; (*c*) an 800×200 grid; (*d*) jetting under a forced numerical stabilization in an self-similar flow for a 600×150 grid. The density contour increments are $\Delta\rho/\rho_0 = 0.3$.

found that the condition corresponds to a singularity of the form

$$\frac{\partial \delta_2}{\partial p_2} \sim (p_2 - p_n)^{-1/2}, \tag{4.12}$$

where δ_2 is the streamline deflection angle across the n_1 shock, p_n is the downstream pressure when n_1 is a normal shock and p_2 is the downstream pressure when it is not normal. Thus, the calculations for the streamline deflection angle and for β_1, become sensitive (they are not robust) to small variations in the system parameters as $\beta_1 \to 90°$, while the pressure calculations remain robust. The sucessive refinements in figure 17 straddle this singularity. As seen in figure 2(*d*) of the Colella & Henderson (1990), the von Neumann theory displays increasing discrepancies with experiment as $\beta_1 \to 90°$. They obtained numerical evidence that the assumption made by von Neumann that there were three shocks of zero thickness meeting at the node, became increasingly in error as $\beta_1 \to 90°$. As β_1 is rather large for our results it may be an alternative explanation as to why they differ from the results of the von Neumann theory.

Finally, if θ_W is decreased continuously from 55° (figure 15*c*) to 50° (figure 15*b*), it is plausible that the supersonic flow downstream of n_1 will decrease continuously through sonic to subsonic; thus causing the n_2-shock to vanish and the system to evolve into that in figure 15(*b*). It is also plausible that the evolution is reversible. By contrast, it seems implausible that during evolution, the system would jump discontinuously to the Mach node configuration at T_1.

4.7. *Wall-jet instability*

A detailed study of the flow instability inside the wall-jet was performed for $M_i = 4.5$ and ramp angle $\theta_w = 36°$. Figures 18(*a*) to 18(*c*) show the unsteady system of

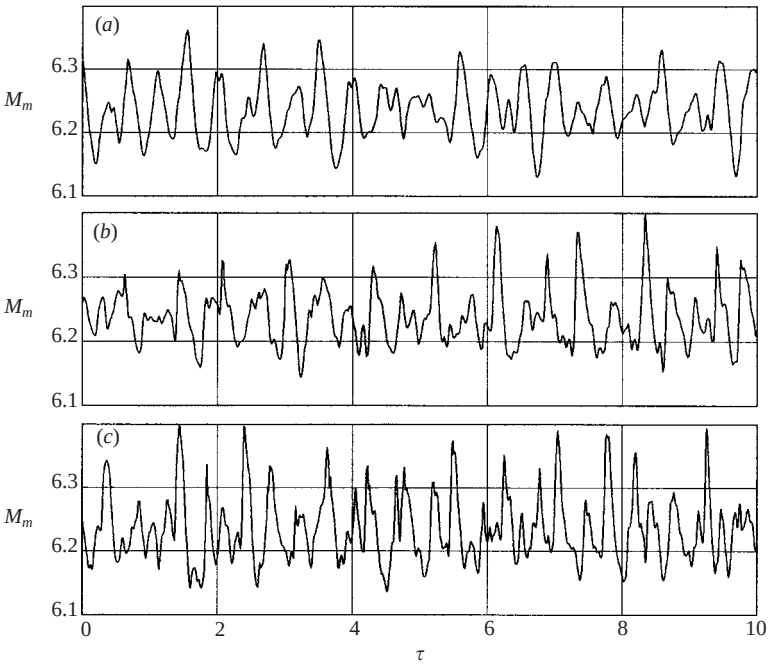

FIGURE 19. Fluctuations of the Mach number at the foot of the n-shock for the unstable flow shown in figure 18 as computed on different grids. (a) 400×100 grid; (b) 600×150 grid; (c) 800×200 grid.

vortices obtained with different grids. The vortices that are formed along the contact discontinuity, grow with time, and propagate into the jet. Note that shedding frequency of the vortices is higher for the finer grid, but the average size of the vortices and the number of them inside the jet do not depend upon the mesh size. This can be explained by the vortex interaction mechanism; namely, before entering the jet, the smaller vortices merge into the larger ones whose sizes are determined by the jet width.

In order to find a reason for the jet instability, it is necessary to determine the self-similar flow numerically. Regularizing algorithms were employed, as is done when solving ill-posed problems. A simple numerical forced stabilization procedure was applied to obtain a stationary solution. Time relaxation was applied at some cells of the moving computational grid.

The increments of flow parameters at time step Δt were multiplied by a small factor of the order of 0.01, at all the mesh cells having numbers equal to multiples of 5 (i.e. 5, 10, 15, ...). Clearly, this procedure does not affect the solution when the flow is stationary. After turning on the forced numerical stabilization procedure for an unstable flow, such as that shown in figure 18(b), the vortex structures dissipated usually after quite a long time, thereafter the flow stabilized and the self-similar regime shown in figure 18(d) was attained. Note that the vortices inside the unstable jet are about twice as large as its width in self-similar flow.

The time dependence of the Mach number, M_m, at the foot of the n-shock for the unstable jetting in figure 18, is shown in figure 19 for three different grids. Each time unit τ corresponds to doubling the size of the flow structure (logarithmic scale). The stationary value of the Mach number at the foot of the n-shock for a stabilized flow,

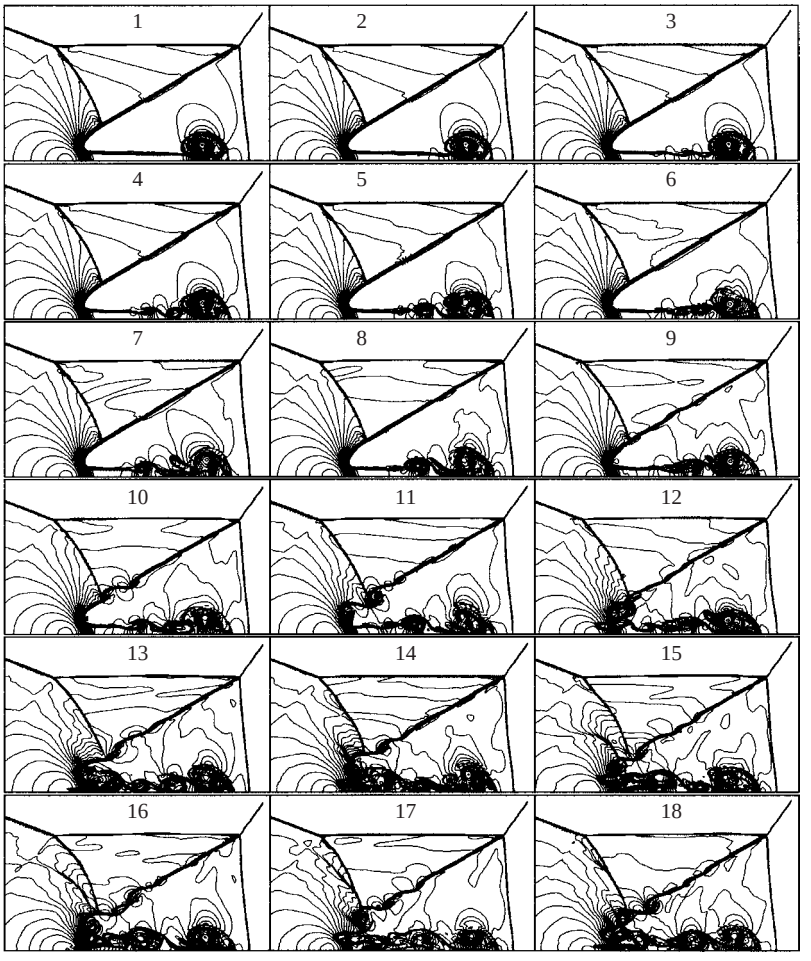

FIGURE 20. Evolution of the flow instability after the removal of the numerical forcing stabilizer.

is $M_m = 6.23$. The fluctuations in time are not periodic because they are caused by interactions between different flow structures (jet, front-vortex, contact discontinuity and shocks), which impose different eigenfrequencies. Although the frequency of the oscillations increases as the number of cells increases, the frequency of the largest oscillations and their amplitudes, depend only weakly on the mesh size. In this case, the amplitude of the variations of the flow parameters at the *n*-shock is not large (only about 8–10% in pressure). This supports the conclusion that the large vortices with sizes of the order of the jet width have the largest effect on the oscillations.

In order to study the instability mechanisms, the stabilized flow shown in figure 18(*d*), was chosen for the initial condition, and the numerical stabilization was turned off. After some time, the flow lost its stability. A time evolution of the self-similar flow losing its stability is shown in figure 20; there are 18 frames of density contours, separated by a constant time increment. Frame 1, is identical to the stable self-similar flow in figure 18*d*, and frame 18 is similar to the unstable flow in figure 18(*b*). An inspection of the frames in figure 20 reveals the following:

Frames 1–3. First appearance of instability at the right end of the jet.

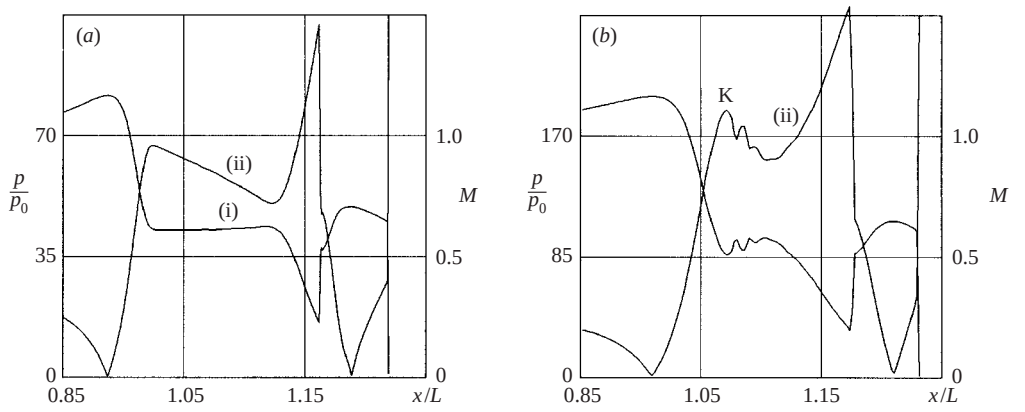

FIGURE 21. Pressure (i) and self-similar Mach number (ii) distributions along the wall in the jet region for self-similar flows. (*a*) $M_i = 4.5$, $\theta_w = 36^\circ$ and $\gamma = 1.4$; (*b*) $M_i = 7$, $\theta_w = 30^\circ$ and $\gamma = 1.3$.

Frames 4–6. The perturbations penetrate the front-vortex and remain there during one period of rotation. The jet and the vortex perturbations grow rapidly, while the left parts of the jet and the contact discontinuity remain stable.

Frames 7–8. The perturbations from the jet-vortex system reach the contact discontinuity and the node.

Frames 9–10. Growing wave perturbations appear at the contact discontinuity, they flow downstream, and curl up into vortices.

Frames 11–12. The vortices grow with time, move into the jet, and destabilize it.

Frames 13–18. The vortices on the contact discontinuity penetrate the jet, interact with the ramp surface, and cause additional shocks. These shocks propagate upstream and interact with the n_1-shock. At the same time, the vortices flow through the jet to the front vortex and cause fluctuations there.

The later irregular evolution of the perturbations may be classified as large-scale turbulence.

This study of the evolving perturbations shows that the instability of the contact discontinuity is caused by perturbations from the vortices inside the jet, and also by pressure oscillations in the front-vortex which occur when the vortices propagating through the jet, reach it. Thus, the instability of the contact discontinuity is an induced effect with respect to the jet instability. Note, that moving the computational domain with a fixed number of cells does not allow resolution of vortices if their size grows more slowly than that of the cells.

Analysing the parameter distributions inside a stabilized jet can assist in understanding the jet instability. The pressure distributions (curves 1) and the self-similar Mach number (curves 2) along the jet are shown for two cases in figures 21(*a*) and 21(*b*). The jet is located between the two points at which the self-similar Mach numbers are zero. Note that the pressure reaches local maximum values at these points. The left-hand point is a stagnation point and the right-hand point is on the boundary of the large vortex. The self-similar Mach number increases rapidly inside the jet, and attains values close to unity or even larger. The maximum value of it at the entrance of the jet is larger than 0.95 in figure 21(*a*). It gradually decreases further

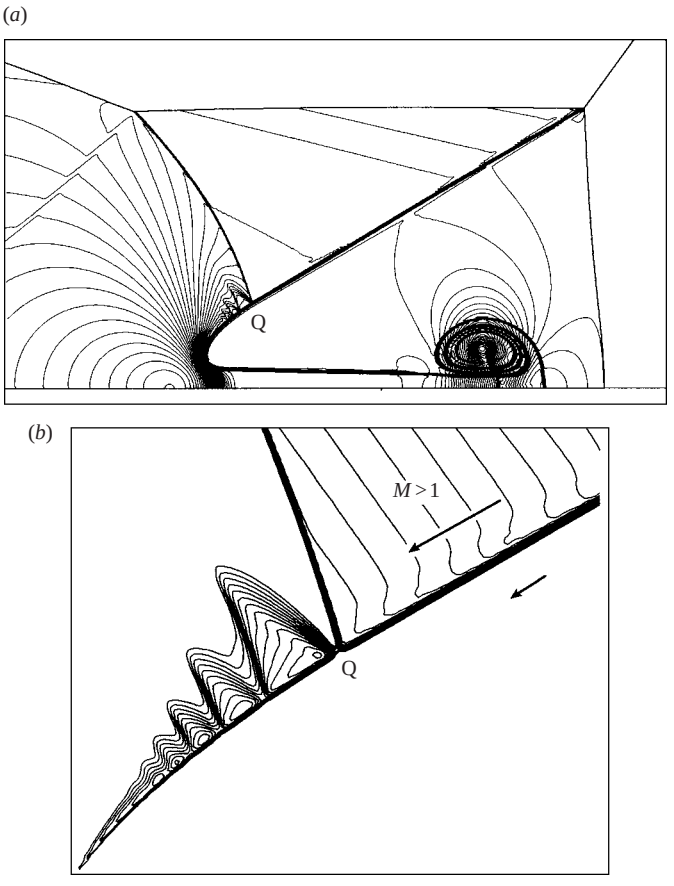

FIGURE 22. Cascade interaction along the contact discontinuity. Adaptive mesh refinement for figure 18(*d*). (*a*) Isopycnics of the forced stable flow. (*b*) Supersonic Mach number contours near the interaction of the n_1-shock and the contact discontinuity.

along the jet, until it begins to increase again near the large vortex. Immediately under this vortex, the flow becomes supersonic, and a shock forms. This is evident by the sudden pressure jump. In figure 21(*b*), the self-similar Mach number at the jet entrance exceeds unity, and local supersonic zones, terminated by weak end waves, are formed. These waves are seen in the pressure distribution immediately downstream of point K. The two cases, shown in figures 21(*a*) and 21(*b*), reveal that the flow in the jet is transonic, i.e. the self-similar Mach number is close to unity. Such jets are known to be unstable because the disturbances propagating upstream have low relative velocities with respect to the jet. As a result, they overtake each other inside the jet and increase their amplitudes. Experimental observations of the instability can be found in Ishii *et al.* (1999). It is important to note that the results indicated that the jet instability effects near the ramp surface appeared when the self-similar Mach number at the jet entrance was nearly sonic.

Whether the fluctuations will occur in actual flows is an open question; variations in the specific heats, the thermal conductivity, and the viscosity, could modify the flow and damp the evolution of the perturbations, or even prevent their occurrence. Although jets are observed in experiments (see e.g. Ben-Dor 1978; Shirouzu & Glass

1982; Glaz *et al.* 1986), it can be expected that because of heat and viscous dissipations, the behaviours of the jet and the front-vortex will be different from those obtained in the inviscid calculations. It is probable that these effects will affect the jet instability.

4.8. *Cascade interaction*

Consider now the numerical stabilization of the solution in more detail. The density contours for a stabilized self-similar flow obtained by using a very refined mesh (1200×400 with local mesh refinement), are shown in figure 22(*a*). The interaction of the n_1-shock with the contact discontinuity at point Q is of special interest. The flow field is stationary in a self-similar frame, and the gas flows from the node towards the n_1-shock with supersonic velocity. The n_1-shock is formed by compression waves that propagate from the ramp surface towards the first node. Consequently, the flow behind this shock must be subsonic. Nevertheless, a rarefaction fan, which cannot exist in a subsonic flow, is seen to emanate from Q in figure 22(*a*). The resolution of this paradox follows from the fact that the flow behind the n_1-shock is subsonic everywhere except at Q, where it is sonic $M = 1$. An enlargement of the flow field, in the vicinity of Q, is shown in figure 22(*b*). A supersonic domain extends from the n_1-shock at Q, and along the contact discontinuity downstream of Q. The rarefaction fan emanating from Q is located inside this domain. Vasilev (1999) showed analytically that the curvature of the wavefront at Q could be infinite, as is the situation in the present case. Inspection of figure 22(*a*) confirms that the n_1-shock is strongly curved near Q. The convergence of the contours downstream of the rarefaction corresponds to a weak compression wave. Alternating rarefaction and compression waves are seen behind this compression. Thus, a cascade of alternating rarefaction and compression waves with decreasing intensity is formed. Near the contact discontinuity the flow decelerates to $M = 1$ for each compression, then accelerates and turns into a rarefaction where the pressure recovers its value before the following compression.

5. Conclusions

The jetting effect in Mach reflection has been investigated numerically and analytically. The numerical model, based on the solution of the Euler equations, revealed that there is no unique correspondence between the kind of shock reflection (single-, transitional-, or double-irregular-reflection) and the occurrence of jetting.

An approximate criterion for the jetting $\leftrightarrow$ no-jetting transition was derived from the equations of motion under the assumptions of self-similarity and radial flow behind the *n*-shock. The criterion was found to be necessary but not sufficient for the onset of the jetting effect.

The jet width, or, more precisely, the size of the vortex at the front of it, is determined by the angle of the *n*-shock at the node, for transitional- and the double-irregular systems.

At smaller ramp angles, $\theta_w \leqslant 15^\circ$, the jet flow was such that its streamlines had no branch or stagnation points on the ramp surface. All the streamlines curled into a vortex at the front of the jet, and the jet was then stable. A streamline branch point did appear when the ramp angle θ_w was increased, but it was not associated with any particular type of system. When θ_w approached the detachment value, the branch point for the streamlines passing through the *i–r* sequence disappeared, and the jet intensity was sharply reduced.

Two types of jetting were identified, namely, strong jetting, which was defined as jetting with a branch point in the streamlines passing through the *i–r* sequence, and weak jetting, defined as jetting without such a point. Weak jetting was possible for both small and large values of θ_w.

Two types of shock reflection system were found for the dual-solution-domain (only regular reflection has been observed in experiments for this domain). They were a system containing a three-shock-Mach-node followed by a four-shock-overtake-node (DIR), and another system, that seemed to be intermediate between the previous one and a three-node-shock-reflection (TIR), which was first hypothesized by Ben-Dor & Glass (1979). These have been previously and incorrectly called a double-Mach-reflection (DMR), and the second a transitional-double-Mach-reflection (TDMR), respectively.

The strong jet and the contact discontinuity were unstable. The primary instability was in the jet. The main reason for the jet instability was that the self-similar Mach number was nearly sonic in the inlet region of the jet. The instability of the contact discontinuity was secondary with respect to the instability of the jet.

The interaction of the n_1-shock with the contact discontinuity in a double-irregular-reflection, resulted in an alternating cascade of rarefaction and compression waves with decreasing intensity along the contact discontinuity.

An adaptive moving grid was essential for the numerical solution of the problem. Tracking the shock fronts and moving grids allowed us to study the flow field for long time intervals. The time interval $0 < \tau < 10$ in figure 19 corresponds to the increase of the size of the perturbed flow by a factor of 2^{10}, or more than a thousand fold. The jet was unstable for almost the entire (DIR) flow and the interaction of the n_1-shock with the contact discontinuity could be studied only by using an artificial stabilization of the flow. Although the latter procedure could be realized on a moving grid, its realization on the stationary grid is an open question.

This study was conducted under the auspices of the Dr Morton and Toby Mower Chair of Shock Wave Studies.

REFERENCES

Abdel-Fattah, A. M. & Henderson, L. F. 1978 *J. Fluid Mech.* **89**, 79–95.

Abdel-Fattah, A. M., Henderson, L. F. & Lozzi, A. 1976 *J. Fluid Mech.* **76**, 157–176.

Ben-Dor, G. 1978 Nonstationary oblique-shock wave reflections in nitrogen and argon: experimental results. *UTIAS Rep.* 237.

Ben-Dor, G. 1991 *Shock Wave Reflection Phenomena.* Springer.

Ben-Dor, G. & Glass, I. I. 1979 Domains and boundaries of nonstationary oblique shock wave reflections. Part 1. Diatomic gas. *J. Fluid. Mech.* **92**, 459–496.

Birkoff, G., MacDougal, D. P., Pugh, E. M. & Taylor, G. I. 1948 Explosives with lined cavities. *J. Appl. Phys.* **19**, 563–582.

Colella, P. & Henderson, L. F. 1990 The von Neumann paradox for the diffraction of weak shock waves. *J. Fluid Mech.* **213**, 71–94.

Dear, J. P. & Field, J. E. 1986 An investigation of the shock structures and conditions for jetting during liquid impact. In *Shock Waves in Condensed Matter* (ed. Y. M. Gupta), Plenum.

Dewey, J. M. & van Netten, A. A. 1991 Observations of the initial stages of the Mach reflection process. In *Shock Waves* (ed. K. Takayama), vol. 1, pp. 227–232. Springer.

Dewey, J. M. & van Netten, A. A. 1995 Non-self-similarity of the initial stages of Mach reflection. In *Shock Waves* (ed. B. Sturtevant, J. E. Shepherd & H. G. Hornung), vol. 1, pp. 399–404. World Scientific.

Glaz, H., Colella, P., Glass, I. I. & Deschambault, R. L. 1985 A numerical study of oblique shock wave reflections with experimental comparisons. *Proc. R. Soc. Lond.* A **398**, 117–140.

Glaz, H. M., Colella, P., Glass, I. I. & Deschambault, R. L. 1986 A detailed numerical, graphical and experimental study of oblique shock wave reflections. *UTIAS Rep.* 285.

Glimm, J., Klingenberg, C., McBryan, O., Plohr, B., Sharp, D. & Yaniv, S. 1985 Front tracking and two-dimensional Riemann problems. *Adv. Appl. Maths* **6**, 259–290.

Hammit, F. G. 1980 *Cavitation and Multi-phase Flow Phenomena.* McGraw-Hill.

Henderson, L. F., Colella, P. & Puckett, E. G. 1991 On the refraction of shock waves at a slow–fast gas interface. *J. Fluid Mech.* **224**, 1–27.

Henderson, L. F., Crutchfield, W. Y. & Virgona, R. J. 1997 The effects of heat conductivity and viscosity of argon on shock waves diffracting over rigid ramps. *J. Fluid Mech.* **331**, 1–36.

Henderson, L. F. & Menikoff, R. 1998 Triple-shock entropy theorem and its consequences. *J. Fluid. Mech.* **366**, 179–210.

Henderson, L. F., Takayma, K., Crutchfield, W. Y. & Itabashi, S. 2001 The persistence of regular reflection during strong shock diffracting over rigid ramps. *J. Fluid Mech.* **431**, 273–296.

Ishii, R., Fujimoto, H., Hatta, N. & Umeda, Y. 1999 Experimental and numerical analysis of circular pulse jets. *J. Fluid Mech.* **392**, 129–153.

Jahn, R. G. 1956 The refraction of shock waves at a gaseous interface. *J. Fluid Mech.* **1**, 457–489.

Jones, D. M., Moira, P., Martin, E. & Thornhill, C. K. 1951 A note on the pseudo-stationary flow behind a strong shock wave diffracted or reflected at a corner. *Proc. R. Soc. Lond.* A **209**, 238–248.

Kieffer, S. W. 1977 Impact condition required for formation of melt by jetting in silicates. In *Impact and Explosion Cratering* (ed. D. J. Roddy, R. O. Pepin & R. B. Merrill), pp. 751–769. Pergamon.

Li, H. & Ben-Dor, G. 1999 Analysis of double-Mach-reflection wave configurations with convexly curved Mach stems. *Shock Waves* **9**, 319– 326.

Meyers, M. A. 1994 *Dynamic Behavior of Materials.* John Wiley.

Olim, M., Dewey, J. M. 1992 A revised three-shock solution for the Mach reflection of weak shock waves. *Shock Waves* **2**, 167–176.

Rinehart, J. S. & Pearson, J. 1963 *Explosive Working of Metals.* Pergamon.

Shirouzu, M. & Glass, I. I. 1982 An assessment of recent results on pseudo-stationary oblique-shock wave reflections. *UTIAS Rep.* 264.

Springer, G. S. 1976 *Erosion by Liquid Impact*. John Wiley.

Vasilev, E. I. 1996 A W-modification of Godunov's method and its application to two-dimensional non-stationary flows of a dusty gas. *Comput. Math. Math. Phys.* **36**, 101–112. Translation from *Z. Vychisl. Mat. Mat. Fiz.* **36**, 122–135.

Vasilev, E. I. 1998 Instability of self-similar ideal gas flows with shock waves. *Fluid Dyn.* **33**, 604–611. Translation from *Izv. RAN, Mekh. Zhidk. i Gaza* **4**, 166–175.

Vasilev, E. I. 1999 Four-wave scheme of weak Mach shock wave interaction under von Neumann paradox conditions. *Fluid Dyn.* **34**, 421–427. Translation from *Izv. RAN, Mekh. Zhidk. i Gaza* **3**, 144–152.

Walsh, J. M., Shreffler, R. G. & Willing, F. J. 1953 *Appl. Phys.* **24**, 349–359.